Surface Curvature Effect on Dual-Atom Site Oxygen Electrocatalysis

Ritums Cepitis,[†] Nadežda Kongi,[∗,†] Jan Rossmeisl,[‡] and Vladislav Ivaništšev[∗,‡]

†Institute of Chemistry, University of Tartu, Ravila 14a, 50411 Tartu, Estonia

‡Department of Chemistry, Center for High Entropy Alloy Catalysis, University of Copenhagen, Universitetsparken 5, 2100 Copenhagen, Denmark

E-mail: nadezda.kongi@ut.ee; vliv@chem.ku.dk

Abstract

Improved oxygen electrocatalysis is crucial for the ever-growing energy demand. Metal-Nitrogen-Carbon (M-N-C) materials are promising candidates for catalysts. Their activity is tunable via varying electronic and geometric properties, such as porosity. Because of the difficulty in modeling porosity, M-N-Cs with variable surface curvature remained largely unexplored. In this work, we developed a realistic in-pore dual-atom site M-N-C model and applied density functional theory to investigate the surface curvature effect on oxygen reduction and evolution reactions. We show that surface curving tailors both scaling relations and energy barriers. Thus, we predict that adjusting the surface curvature can improve the catalytic activity toward mono- and bifunctional oxygen electrocatalysis.

Metal-Nitrogen-Carbon (M-N-C) catalysts are promising candidates to reduce reliance on expensive platinum-group metals and achieve reliable activity for oxygen reduction and evolution reactions (ORR/OER).[1–5] The main feature of M-N-C catalysts is their porous structure with single-atom sites, providing an adjustable site environment and efficient atom

1

usage.[6,7] Density functional theory (DFT) has highlighted the principal limitations in the development of new M-N-C catalysts.[8,9] For ORR and OER, the main limitation is the scaling relation for two key intermediates, OH and OOH.[10–14]

Figure 1 illustrates the evolution of M-N-C models that address the OH–OOH scaling relation at the DFT level. Changing the metal in **model (a)** – a single-atom site catalyst – simultaneously and proportionally varies the adsorption energies of all intermediates; thus, it is limited by the OH–OOH scaling relation.[15] Changing the adjacent metals in **model (b)** – a dual-atom site catalyst – also controls the adsorption energies and still follows the OH–OOH scaling relation.[16] Changing the geometry of **model (c)** – a dual-atom site catalyst – enables an alternative reaction mechanism that excludes OOH and switches the scaling relation.[17–20] However, this artificial model requires impractical atomic-level control to make a real electrode. **Model (d)** is an in-pore dual-atom site catalyst that also switches the scaling relation to a more favorable one while providing more precise control of all adsorption energies. Moreover, the synthetic realization of **model (d)** can employ the intrinsic properties of M-N-C materials, such as inter-site distance and surface curvature.

The effects of inter-site distance and surface curvature on electrocatalytic activity have been discovered recently.[21–23] On the one hand, the previously reported surface curvature effect mimics the well-known strain effect.[24] On the other hand, to the best of our knowledge, the surface curvature effect that enhances dual-atom site catalysis remains unknown. Porous carbon materials, such as M-N-Cs, are ideal candidates to investigate this effect because they are inherently curved.[25–28] A significant fraction of double-atom sites among randomly distributed single-atom sites is visible in many M-N-C materials, for example, in microscopic images in Refs.[29,30] Hypothetically, optimizing surface curvature and inter-site distance of M-N-Cs can change the reaction mechanism and increase the OER/ORR activity.

This work presents a realistic in-pore dual-atom site M-N-C model that relates surface curvature to the activity of ORR and OER beyond the OH–OOH scaling relation limitations.
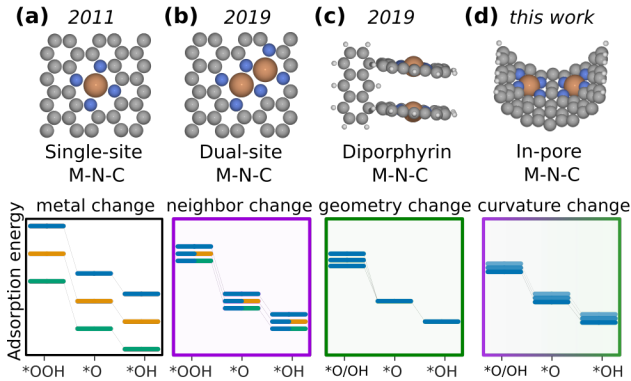
Figure 1: Timeline of the M-N-C model development. The adsorption energies of intermediates vary with changing (a) M in the flat single-atom site model,[15] (b) second M in the flat dual-atom site model,[16] (c) geometry of the diporphyrin model,[19] and (d) surface curvature of the in-pore model. Line color indicates a different M, line transparency indicates distinct geometry.

In-pore dual-atom site model The surface curvature is a parameter common for all porous carbon materials. More specifically, for nanotubes and cylindrical pores, the surface curvature is the inverse of the inner radius (r). Our curved models (r = 4, 6, 8, 8.5 Å) represent the extent of surface curvature within micropores, while the flat model (with $r = \infty$) is a reference point for the usual adsorption behavior. To construct the models, we start with an armchair nanoribbon, introduce two MeN_4 sites, and then curve the surface to the desired radius as shown in Figure 2. We considered two models: with two CoN_4 sites and with CoN_4 plus NiN_4 site. These models are further referred to as CoCo and CoNi models, respectively. Cobalt was chosen based on existing information on optimal adsorption energies on single-site catalysts; nickel was chosen as a lesser binding site to compare the effect of the secondary site.[15]

3
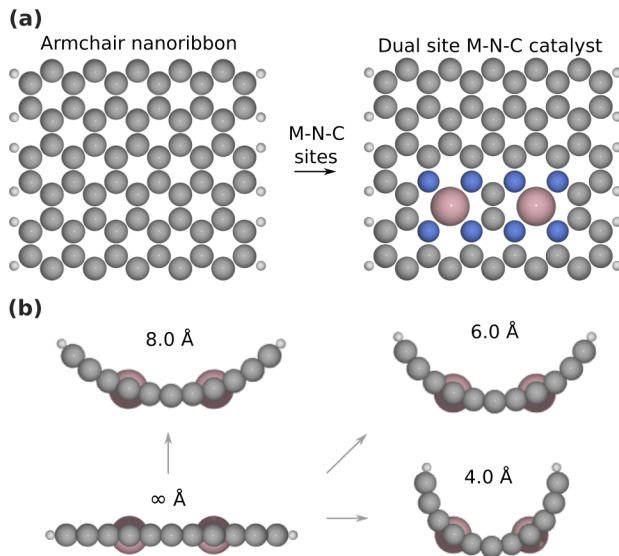
Figure 2: (a) Top view on constructing a dual-atom site M-N-C model from an armchair nanoribbon. (b) Side view on curving the flat dual-atom M-N-C model into in-pore models.

Surface curvature and the adsorption energies The surface curvature affects the adsorption energy of each ORR intermediate within both associative and dissociative mechanisms (Figure 3(a)). The dependence of ΔG_{OOH} and $\Delta G_{\text{O/OH}}$ on the pore radius in Figure 3(b,c) has two components.

First – the metal effect on adsorption energy. Black bars in Figure 3(b,c) indicate similar ΔG_{OOH} adsorption energies for CoCo and CoNi models at equal radii. That is expected for the associative mechanism due to the weak neighboring effect and the preferable strong binding of OOH to the CoN_4 site. In contrast, colored and white bars in Figure 3(b,c) indicate lower $\Delta G_{\text{O/OH}}$ adsorption energies for the CoCo model than for the CoNi model at equal radii. That is expected for the dissociative mechanism because of the weak binding of OH to the NiN_4 site.

Second – the curvature effect on adsorption energy. Data in Figure 3(a–b) shows a clear trend of decreasing adsorption energies with increasing radius. The decrease correlates with a change in electronic structure upon curving (see the density of states analysis in the SI). The decrease is steeper for dissociative than for associative mechanisms because

4

of the simultaneous adsorption of two intermediates (O and OH) rather than one (OOH). Above all, curving the CoCo model surface from flat to 8 Å adjusts the adsorption energy to the ideal value of 3.69 eV (green horizontal line). Nevertheless, in addition to reaching an ideal adsorption energy, it is more important to adjust the energy differences for efficient catalysis.
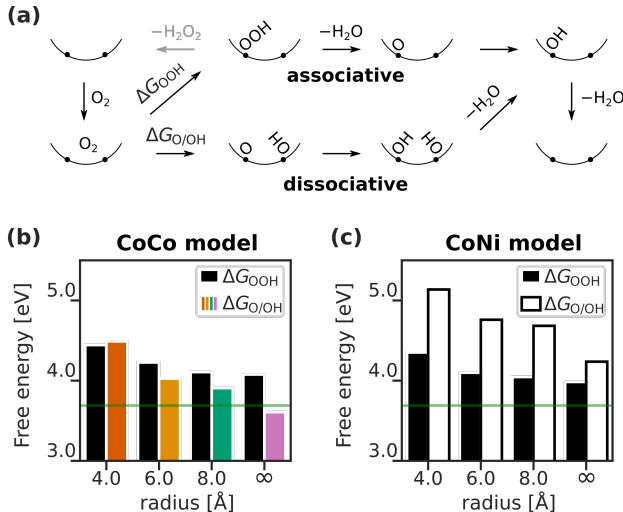
Figure 3: First ORR intermediate adsorption energy for associative and dissociative mechanisms: (a) Schematic drawing of both mechanisms, (b) CoCo model energies, and (c) CoNi model energies. The green line indicates the ideal adsorption energy.

Surface curvature and the scaling relations   For the dissociative mechanism, surface curving allows adjusting the difference between the adsorption energies of two intermediates. Figure 4 shows the dependence of $\Delta G_{O/OH} - \Delta G_{OH}$ and $\Delta G_{OOH} - \Delta G_{OH}$ on the inter-site distance which is inverse proportionality to the squared pore radius (for derivation, see the SI):

$$d_r = d_\infty - \frac{1}{24} \cdot \frac{d_\infty^3}{r^2} \tag{1}$$

where d_r is distance at radius r and d_∞ is the inter-site distance on flat surface.

For the associative mechanism, the free energy difference is almost independent of the pore radius and is close to the expected OH–OOH scaling relation of 3.2 eV. On the contrary, for the dissociative mechanism, there is a clear $\Delta G \sim r^{-2}$ linear dependence. Moreover, for

the CoCo model, the switch of scaling relations allows going below $3.2\,\mathrm{eV}$ and approaching the ideal difference of $2.46\,\mathrm{eV}$. However, that is not enough for an ideal catalyst, as the dissociative reaction overpotential also depends on O and OH/OH intermediates in addition to OH O/OH.
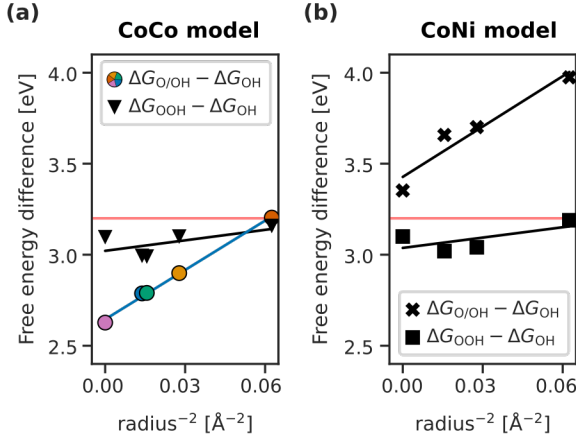
Figure 4: The linearized plot of free energy differences vs. the inter-site distance which is expressed as r^{-2}. Using colored points as a reference, the pore radius of the CoCo model is respectively ∞, 8.5, 8.0, 6.0, and 4.0 Å from left to right.

Surface curvature and climbing of overpotential volcanoes In Figure 5, we plot the 3D ORR overpotential heatmap (volcano)[19] and further generalize it to OER and bifunctional overpotentials. The ORR overpotential in terms of intermediate adsorption energies is defined as

$$\eta_{\mathrm{ORR}} = 1.23\,\mathrm{V} - \min(4.92 - \Delta G_{\mathrm{OOH}},\ \Delta G_{\mathrm{OOH}} - \Delta G_{\mathrm{O}},$$
$$\Delta G_{\mathrm{O}} - \Delta G_{\mathrm{OH}},\ \Delta G_{\mathrm{OH}})/e \tag{2}$$

and for OER

$$\eta_{\mathrm{OER}} = \max(4.92 - \Delta G_{\mathrm{OOH}},\ \Delta G_{\mathrm{OOH}} - \Delta G_{\mathrm{O}},$$
$$\Delta G_{\mathrm{O}} - \Delta G_{\mathrm{OH}},\ \Delta G_{\mathrm{OH}})/e - 1.23\,\mathrm{V} \tag{3}$$

with bifunctional overpotential $\eta_{\mathrm{bifunc}} = \eta_{\mathrm{ORR}} + \eta_{\mathrm{OER}}$. These expressions and the assumption that $\Delta G_{\mathrm{OH}} \approx 2\Delta G_{\mathrm{O}}$ define the contours in Figure 2.[19]

The black data points (for the associative mechanism) are situated around the comparison

6

line which represents MeN_4 energies from Ref.[15] and obeys the OH–OOH scaling relation.

The colored data points (for the dissociative mechanism on the CoCo model) follow a dashed line characteristic for the OH–O/OH scaling relation.[19] With increasing pore radius, this line enters the low-overpotential region. For ORR in Figure 5(a), the dashed line is only 0.15 V far from the volcano top when the pore radius is slightly above 8 Å. With OER in Figure 5(b), the situation is different, as the volcano shows a steeper dropoff of overpotentials than for ORR, and the predicted radius–energy relationship does not improve the OER activity as significantly. Overall, the resulting bifunctional activity is highest, with the models having pore sizes of 8.0 Å and 8.5 Å.
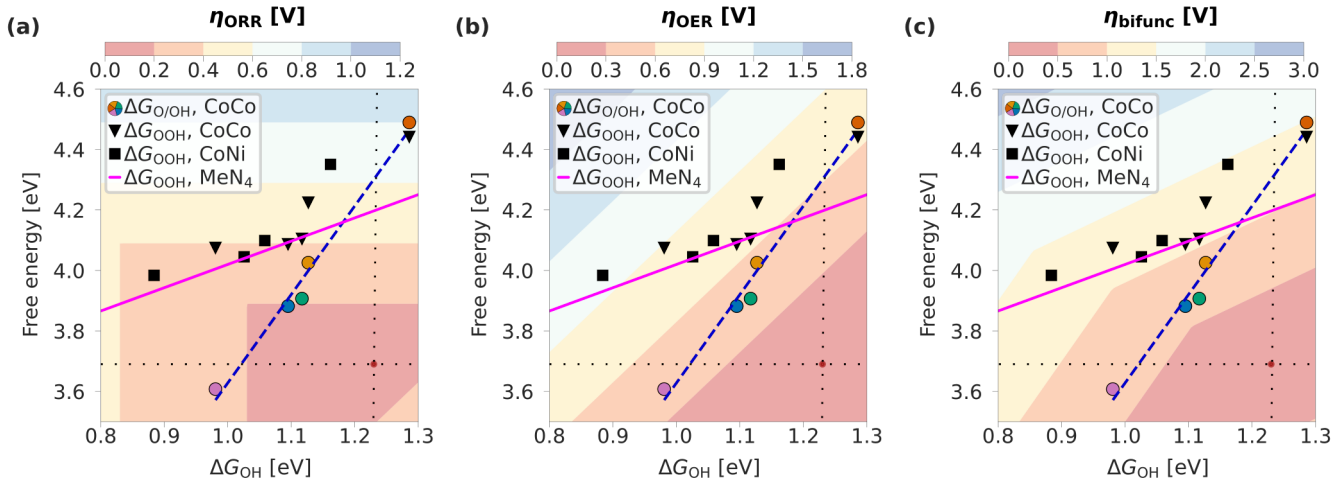
Figure 5: 3D overpotential heatmaps (volcanoes) for (a) ORR, (b) OER, and (c) bifunctional overpotentials. Using colored points as a reference, the pore radius of the CoCo model is respectively ∞, 8.5, 8.0, 6.0, and 4.0 Å from left to right. The volcano tops ($\eta = 0$ V) are marked with a dot at the crossing of thin dotted lines.

Surface curvature and the overpotential of reactions In Figure 6, we compare the overpotentials for bifunctional oxygen catalysis on a complete free energy diagram. It shows that increasing the pore radius from 8.0 Å to 8.5 Å decreases the η_{ORR}, but increases the η_{OER}. As a result, the optimal $\eta_{bifunc} = 0.45$ V is achieved around $r = 8.5$ Å.

Note that the bifunctional overpotential is significantly lower than indicated by the overpotential volcano shown in Figure 5(c). More specifically, η_{OER} in Figure 5(b)is around 0.4 V,

whether the directly calculated overpotential is 0.25 V. In general, more precise overpotential calculations (Figure 6) predict even higher activity than those given by the approximation $\Delta G_{\mathrm{OH}} \approx 2\Delta G_{\mathrm{O}}$ (Figure 4).
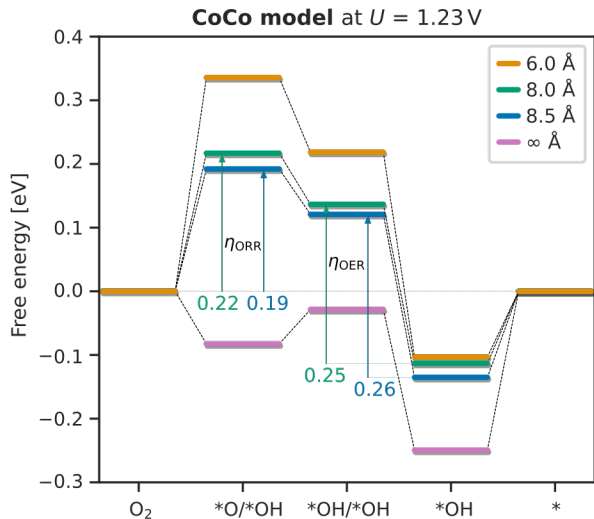
Figure 6: Free energy diagram for the ORR dissociative mechanism. Results were obtained at the CoCo model with variable pore radius and at an equilibrium potential of 1.23 V.

Surface curvature and the dissociation barrier   As shown above, the OOH dissociation to O/OH switches scaling relation from OH–OOH to a more favorable OH–O/OH, and theoretically increase the activity. The dissociation also excludes the $2e^-$ reduction to H_2O_2, which is known to affect the ORR selectivity at single-atom site catalysts.[31,32] However, both activity and selectivity depend on the reaction kinetics. Data in Table 1 indicate that surface curving affects a key parameter in reaction kinetics – the dissociation barrier. On a plane surface ($r = \infty$), the dissociation is thermodynamically favorable, but a high barrier makes it improbable. On a strongly curved surface ($r = 4.0$ Å), the dissociation is thermodynamically unfavorable (due to intermediate repulsion), while the barrier is favorably low. In between, the dissociation is thermodynamically favorable, and the dissociation barrier grows with increasing pore radius. Hence, moderate curving can effectively balance kinetics (Table 1), thermodynamics (Figures 3–4), catalytic activity (Figures 5–6), and selectivity (Figure 3a).

Table 1: Results of nudged elastic band (NEB) calculations for the dissociation of OOH to O/OH. Results obtained at the CoCo model with variable pore radius (r). G_a is the activation barrier; $\Delta G = \Delta G_{O/OH} - \Delta G_{OOH}$ is the dissociation reaction free energy.

r [Å]	G_a [eV]	ΔG [eV]
∞	0.97	-0.45
8.5	0.78	-0.19
8.0	0.68	-0.18
6.0	0.51	-0.18
4.0	0.32	0.07

Discussion and Conclusions   Using DFT calculations, we found that optimizing the surface curvature can reduce the ORR overpotential below 0.20 V and achieve bifunctional overpotential as low as 0.45 V, *i. e.* lower than 0.74 V set by the OH–OOH scaling relation. The finding promises an advance in (bifunctional) oxygen electrocatalysis in fuel cells, electrolyzers, and air-batteries.

We show that changing the mechanism and stabilizing the intermediates switches the scaling relation from OH–OOH (limiting the overpotentials to 0.37 V) to OH–O/OH (limiting the overpotentials to 0.15 V). The first way is well-known,[19,33] while the second one – stabilization by means of surface curving – is demonstrated for the first time.

The curvature effect remained unknown because curved models are rare due to their peculiar geometry and periodicity (cf. Ref.[34]). The presented dual-atom site model has adjustable curvature and realistic periodicity, and suits future studies on in-depth aspects of in-pore electrocatalysis, such as stabilization via oxophilic spectator ligands and microkinetic modeling.[33,35]

We suggest verifying the surface curvature effect at M-N-C catalysts by varying inter-site distance and pore radius. Distributions of these two intrinsic properties of porous M-N-Cs can be regulated by the synthesis conditions. Novel M-N-C catalysts can be, in principle, made with natural curving and randomly allocated in-pore dual-atom sites, unlike nanotubes, which are synthesized with specific radii and regularly allocated out-pore single-atom sites.[36–40]

Acknowledgement

Supporting Information Available

Computational details, description of the in-pore dual-atom site model, PDoS analysis, BEE error estimation, NEB analysis, and Table of all binding energies used in this work. Model structures, total energies, and analysis scripts are available on the webpage `https://nano.ku.dk/english/research/theoretical-electrocatalysis/katladb/surface-curvature-effect-on-`

References

(1) Seh, Z. W.; Kibsgaard, J.; Dickens, C. F.; Chorkendorff, I.; Nørskov, J. K.; Jaramillo, T. F. Combining Theory and Experiment in Electrocatalysis: Insights into Materials Design. *Science* **2017**, *355*, eaad4998.

(2) Peng, L.; Shang, L.; Zhang, T.; Waterhouse, G. I. N. Recent Advances in the Development of Single-Atom Catalysts for Oxygen Electrocatalysis and Zinc–Air Batteries. *Adv. Energy Mater.* **2020**, *10*, 2003018.

(3) Wang, M.; Yang, W.; Li, X.; Xu, Y.; Zheng, L.; Su, C.; Liu, B. Atomically Dispersed

Fe–Heteroatom (N, S) Bridge Sites Anchored on Carbon Nanosheets for Promoting Oxygen Reduction Reaction. *ACS Energy Lett.* **2021**, *6*, 379–386.

(4) Luo, M.; Sun, W.; Xu, B. B.; Pan, H.; Jiang, Y. Interface Engineering of Air Electrocatalysts for Rechargeable Zinc–Air Batteries. *Adv. Energy Mater.* **2021**, *11*, 2002762.

(5) Debe, M. K. Electrocatalyst Approaches and Challenges for Automotive Fuel Cells. *Nature* **2012**, *486*, 43–51.

(6) He, Y.; Liu, S.; Priest, C.; Shi, Q.; Wu, G. Atomically Dispersed Metal–Nitrogen–Carbon Catalysts for Fuel Cells: Advances in Catalyst Design, Electrode Performance, and Durability Improvement. *Chem. Soc. Rev.* **2020**, *49*, 3484–3524.

(7) Shi, Z.; Yang, W.; Gu, Y.; Liao, T.; Sun, Z. Metal-Nitrogen-Doped Carbon Materials as Highly Efficient Catalysts: Progress and Rational Design. *Adv. Sci.* **2020**, *7*, 2001069.

(8) Calle-Vallejo, F.; Loffreda, D.; Koper, M. T. M.; Sautet, P. Introducing Structural Sensitivity into Adsorption–Energy Scaling Relations by Means of Coordination Numbers. *Nat. Chem.* **2015**, *7*, 403–410.

(9) Darby, M. T.; Stamatakis, M.; Michaelides, A.; Sykes, E. C. H. Lonely Atoms with Special Gifts: Breaking Linear Scaling Relationships in Heterogeneous Catalysis with Single-Atom Alloys. *J. Phys. Chem. Lett.* **2018**, *9*, 5636–5646.

(10) Wan, H.; Jensen, A. W.; Escudero-Escribano, M.; Rossmeisl, J. Insights in the Oxygen Reduction Reaction: From Metallic Electrocatalysts to Diporphyrins. *ACS Catal.* **2020**, *10*, 5979–5989.

(11) Divanis, S.; Kutlusoy, T.; Ingmer Boye, I. M.; Man, I. C.; Rossmeisl, J. Oxygen Evolution Reaction: A Perspective on a Decade of Atomic Scale Simulations. *Chem. Sci.* **2020**, *11*, 2943–2950.

(12) Pérez-Ramírez, J.; López, N. Strategies to Break Linear Scaling Relationships. *Nat. Catal.* **2019**, *2*, 971–976.

(13) Huang, Z.-F.; Song, J.; Dou, S.; Li, X.; Wang, J.; Wang, X. Strategies to Break the Scaling Relation toward Enhanced Oxygen Electrocatalysis. *Matter* **2019**, *1*, 1494–1518.

(14) Govindarajan, N.; García-Lastra, J. M.; Meijer, E. J.; Calle-Vallejo, F. Does the Breaking of Adsorption-Energy Scaling Relations Guarantee Enhanced Electrocatalysis? *Curr. Opin. Electrochem.* **2018**, *8*, 110–117.

(15) Calle-Vallejo, F.; Martínez, J. I.; Rossmeisl, J. Density Functional Studies of Functionalized Graphitic Materials with Late Transition Metals for Oxygen Reduction Reactions. *Phys. Chem. Chem. Phys.* **2011**, *13*, 15639–15643.

(16) Meng, Y.; Yin, C.; Li, K.; Tang, H.; Wang, Y.; Wu, Z. Improved Oxygen Reduction Activity in Heteronuclear FeCo-Codoped Graphene: A Theoretical Study. *ACS Sustainable Chem. Eng.* **2019**, *7*, 17273–17281.

(17) Busch, M.; Halck, N. B.; Kramm, U. I.; Siahrostami, S.; Krtil, P.; Rossmeisl, J. Beyond the Top of the Volcano? – A Unified Approach to Electrocatalytic Oxygen Reduction and Oxygen Evolution. *Nano Energy* **2016**, *29*, 126–135.

(18) Pedersen, A.; Barrio, J.; Li, A.; Jervis, R.; Brett, D. J. L.; Titirici, M. M.; Stephens, I. E. L. Dual-Metal Atom Electrocatalysts: Theory, Synthesis, Characterization, and Applications. *Adv. Energy Mater.* **2022**, *12*, 2102715.

(19) Wan, H.; Østergaard, T. M.; Arnarson, L.; Rossmeisl, J. Climbing the 3D Volcano for the Oxygen Reduction Reaction Using Porphyrin Motifs. *ACS Sustain. Chem. Eng.* **2019**, *7*, 611–617.

(20) McGuire Jr., R.; Dogutan, D. K.; Teets, T. S.; Suntivich, J.; Shao-Horn, Y.; Nocera, D. G. Oxygen Reduction Reactivity of Cobalt(Ii) Hangman Porphyrins. *Chem. Sci.* **2010**, *1*, 411–414.

(21) Jin, Z.; Li, P.; Meng, Y.; Fang, Z.; Xiao, D.; Yu, G. Understanding the Inter-Site Distance Effect in Single-Atom Catalysts for Oxygen Electroreduction. *Nat. Catal.* **2021**, *4*, 615–622.

(22) Tang, J.; Zeng, Z.; Liang, H.; Wang, Z.; Nong, W.; Yang, Z.; Qi, C.; Qiao, Z.; Li, Y.; Wang, C. Simultaneously Enhancing Catalytic Performance and Increasing Density of Bifunctional CuN_3 Active Sites in Dopant-Free 2D $C_3 N_3 Cu$ for Oxygen Reduction/Evolution Reactions. *ACS Omega* **2022**, *7*, 19794–19803.

(23) Wang, Y.; Bao, Z.; Shi, M.; Liang, Z.; Cao, R.; Zheng, H. The Role of Surface Curvature in Electrocatalysts. *Eur. J. Chem.* **2022**, *28*, e202102915.

(24) Khorshidi, A.; Violet, J.; Hashemi, J.; Peterson, A. A. How strain can break the scaling relations of catalysis. *Nat. Catal.* **2018**, *1*, 263–268.

(25) Gong, X. et al. Self-Templated Hierarchically Porous Carbon Nanorods Embedded with Atomic Fe-N4 Active Sites as Efficient Oxygen Reduction Electrocatalysts in Zn-Air Batteries. *Adv. Funct. Mater.* **2021**, *31*, 2008085.

(26) Xu, H.; Wang, D.; Yang, P.; Du, L.; Lu, X.; Li, R.; Liu, L.; Zhang, J.; An, M. A Hierarchically Porous Fe-N-C Synthesized by Dual Melt-Salt-Mediated Template as Advanced Electrocatalyst for Efficient Oxygen Reduction in Zinc-Air Battery. *Appl. Catal. B* **2022**, *305*, 121040.

(27) Jung, J. Y.; Kim, S.; Kim, J.-G.; Kim, M. J.; Lee, K.-S.; Sung, Y.-E.; Kim, P.; Yoo, S. J.; Lim, H.-K.; Kim, N. D. Hierarchical Porous Single-Wall Carbon Nanohorns with Atomic-Level Designed Single-Atom Co Sites toward Oxygen Reduction Reaction. *Nano Energy* **2022**, *97*, 107206.

(28) Liu, Y.; Chen, Z.; Li, Z.; Zhao, N.; Xie, Y.; Du, Y.; Xuan, J.; Xiong, D.; Zhou, J.; Cai, L.; Yang, Y. CoNi Nanoalloy-Co-N4 Composite Active Sites Embedded in Hierarchical Porous Carbon as Bi-Functional Catalysts for Flexible Zn-air Battery. *Nano Energy* **2022**, *99*, 107325.

(29) Luo, X.; Wei, X.; Wang, H.; Gu, W.; Kaneko, T.; Yoshida, Y.; Zhao, X.; Zhu, C. Secondary-Atom-Doping Enables Robust Fe–N–C Single-Atom Catalysts with Enhanced Oxygen Reduction Reaction. *Nano-Micro Lett.* **2020**, *12*, 163.

(30) He, X.; He, Q.; Deng, Y.; Peng, M.; Chen, H.; Zhang, Y.; Yao, S.; Zhang, M.; Xiao, D.; Ma, D.; Ge, B.; Ji, H. A versatile route to fabricate single atom catalysts with high chemoselectivity and regioselectivity in hydrogenation. *Nat. Commun.* **2019**, *10*, 3663.

(31) Wang, K.; Huang, J.; Chen, H.; Wang, Y.; Song, S. Recent advances in electrochemical 2e oxygen reduction reaction for on-site hydrogen peroxide production and beyond. *Chem. Commun.* **2020**, *56*, 12109–12121.

(32) Wang, N.; Ma, S.; Zuo, P.; Duan, J.; Hou, B. Recent Progress of Electrochemical Production of Hydrogen Peroxide by Two-Electron Oxygen Reduction Reaction. *Adv. Sci.* **2021**, *8*, 2100076.

(33) Sours, T.; Patel, A.; Nørskov, J.; Siahrostami, S.; Kulkarni, A. Circumventing Scaling Relations in Oxygen Electrochemistry Using Metal–Organic Frameworks. *J. Phys. Chem. Lett.* **2020**, *11*, 10029–10036.

(34) Xie, Y.; Wang, Z.-W.; Zhu, T.-Y.; Shu, D.-J.; Hou, Z.-F.; Terakura, K. Breaking the Scaling Relations for Oxygen Reduction Reaction on Nitrogen-Doped Graphene by Tensile Strain. *Carbon* **2018**, *139*, 129–136.

(35) Wang, Y.; Tang, Y.-J.; Zhou, K. Self-Adjusting Activity Induced by Intrinsic Reaction Intermediate in Fe–N–C Single-Atom Catalysts. *J. Am. Chem. Soc.* **2019**, *141*, 14115–14119.

(36) Li, L.; Yang, H.; Miao, J.; Zhang, L.; Wang, H.-Y.; Zeng, Z.; Huang, W.; Dong, X.; Liu, B. Unraveling Oxygen Evolution Reaction on Carbon-Based Electrocatalysts: Effect of Oxygen Doping on Adsorption of Oxygenated Intermediates. *ACS Energy Lett.* **2017**, *2*, 294–300.

(37) Rathinavel, S.; Priyadharshini, K.; Panda, D. A review on carbon nanotube: An overview of synthesis, properties, functionalization, characterization, and the application. *Mater. Sci. Eng. B* **2021**, *268*, 115095.

(38) Neuhaus, P.; Cnossen, A.; Gong, J. Q.; Herz, L. M.; Anderson, H. L. A Molecular Nanotube with Three-Dimensional π-Conjugation. *Angew. Chem. Int. Ed.* **2015**, *54*, 7344–7348.

(39) Hijazi, I.; Bourgeteau, T.; Cornut, R.; Morozan, A.; Filoramo, A.; Leroy, J.; Derycke, V.; Jousselme, B.; Campidelli, S. Carbon Nanotube-Templated Synthesis of Covalent Porphyrin Network for Oxygen Reduction Reaction. *J. Am. Chem. Soc.* **2014**, *136*, 6348–6354.

(40) Li, J.-C.; Yang, Z.-Q.; Tang, D.-M.; Zhang, L.; Hou, P.-X.; Zhao, S.-Y.; Liu, C.; Cheng, M.; Li, G.-X.; Zhang, F.; Cheng, H.-M. N-doped carbon nanotubes containing a high concentration of single iron atoms for efficient oxygen reduction. *NPG Asia Mater.* **2018**, *10*, e461–e461.

TOC Graphic

optimum radius for the best catalyst

$\eta_{ORR} \to 0.15$ V

Curving

$\eta_{ORR} > 0.34$ V

ORR

OER